

The effect of interstitial carbon atoms on defect evolution in high entropy alloys under helium irradiation



Zhengxiong Su^a, Tan Shi^a, Jinxue Yang^a, Huahai Shen^b, Zhiming Li^c, Sheng Wang^{a,*}, Guang Ran^{d,*}, Chenyang Lu^{a,e,**}

^a Department of Nuclear Science and Technology, Xi'an Jiaotong University, Xi'an 710049, China

^b Institute of Nuclear Physics and Chemistry, China Academy of Engineering Physics, Mianyang 621900, China

^c School of Materials Science and Engineering, Central South University, Changsha 410083, China

^d College of Energy, Xiamen University, Xiamen 361102, China

^e State Key Laboratory of Multiphase Flow in Power Engineering, Xi'an Jiaotong University, Xi'an 710049, China

ARTICLE INFO

Article history:

Received 10 September 2021

Revised 10 April 2022

Accepted 14 April 2022

Available online 20 April 2022

Keywords:

High-entropy alloys

Helium bubbles

Interstitial carbon atoms

Radiation-induced segregation

Irradiation hardening

ABSTRACT

In this work, a design strategy based on a typical multi-principal element alloy ($\text{Fe}_{50}\text{Mn}_{30}\text{Co}_{10}\text{Cr}_{10}$, at. %) was proposed to tune the irradiation behavior by adding interstitial carbon atoms ($\text{Fe}_{49.5}\text{Mn}_{30}\text{Co}_{10}\text{Cr}_{10}\text{C}_{0.5}$, at. %). Advanced scanning transmission electron microscopy was employed to study the evolution of dislocation loops and helium bubbles in alloys after 400 keV He^+ ion irradiation at three different temperatures ranging from 350 °C to 450 °C. The results showed that the interstitial carbon atoms inhibited the growth of He bubbles and irradiation hardening. The high-resolution energy dispersive spectroscopy mapping revealed that the segregation at the dislocation loops in $\text{Fe}_{49.5}\text{Mn}_{30}\text{Co}_{10}\text{Cr}_{10}\text{C}_{0.5}$ was efficiently lessened compared to that in $\text{Fe}_{50}\text{Mn}_{30}\text{Co}_{10}\text{Cr}_{10}$, which shows an even superior performance than the equiatomic FeMnCoCrNi Cantor alloy. Radiation-induced "W-shaped" elemental oscillation patterns with a width of about 1 nm around dislocation loops, were observed for the first time in high-entropy alloys. Such nanoscale local elemental fluctuations are suggested to modify the lattice friction and thus have an impact on the mechanical properties of the material. First-principles calculations suggest that the interstitial carbon atoms can effectively enhance the site-to-site local lattice distortion and modify vacancy migration energy near carbon atoms. Our systematic experiments demonstrate that adding interstitial carbon atoms into multi-principal element or high-entropy alloy is beneficial for the reduction in irradiation hardening and volumetric swelling, as well as radiation-induced segregation.

© 2022 Acta Materialia Inc. Published by Elsevier Ltd. All rights reserved.

1. Introduction

With the increase in demand for global energy and the increasing awareness of the need for environmental protection, advanced nuclear energy systems with higher inherent safety, less radioactive waste, and increased efficiency have attracted significant attention worldwide. In recent years, the focus of various fields has turned to multi-principal element alloys (MPEAs) or high-entropy alloys (HEAs), as they open up a new frontier for the design of new materials with distinct features [1–5]. The definition of HEAs is broadened as exploration continues, and solid solution alloys con-

taining four or more principal elements are commonly referred to as HEAs [6].

Varying the type and number of elements in the HEAs to influence defect evolution is a common approach to investigate the irradiation behavior [7–9]. Lu et al. proposed that the increased number of elements can alter the pattern of irradiation-induced defects to promote defect recombination [7]. Nevertheless, increasing the number of principal elements does not always result in significant changes in the mechanical properties and irradiation response of HEAs [10,11]; meanwhile, it leads to higher manufacturing costs [12]. There are certain intrinsic features of HEAs that have not yet been fully activated and exploited.

The search for a cost-effective strategy to improve the irradiation behavior in HEAs is a must for future nuclear industry production. The inclusion of modest interstitial or alloying elements to improve the material characteristics is an effective method. Li et al. employed minor carbon interstitial atoms into

* Corresponding authors.

** Corresponding author at: Department of Nuclear Science and Technology, Xi'an Jiaotong University, Xi'an 710049, China.

E-mail addresses: shengwang@mail.xjtu.edu.cn (S. Wang), gran@xmu.edu.cn (G. Ran), chenylu@xjtu.edu.cn (C. Lu).

the $\text{Fe}_{50}\text{Mn}_{30}\text{Co}_{10}\text{Cr}_{10}$ (at. %) HEA, which significantly improved the mechanical properties and phase stability of the alloy, owing to the benefits from the combination of interstitial solid solution strengthening and massive substitutional alloy element strengthening [13]. For equiatomic FeMnCoCrNi HEA, a good compromise has been established between strength and plasticity, with skillful management of interstitial carbon atoms to modify the microstructural features and trigger distinct deformation mechanisms [14,15].

The interstitial carbon atoms can effectively interact with point defects in conventional alloys to influence irradiation evolution [16,17]. Recently, Shen et al. studied the effect of carbon atoms in $\text{Fe}_{38}\text{Mn}_{40}\text{Ni}_{11}\text{Al}_4\text{Cr}_7$ (at. %) using 5 MeV Xe^{23+} ions at room temperature, and found that the growth of dislocation loops and irradiation hardening could be suppressed by increasing carbon concentration [18]. However, the behavior of the injected Xe gas bubbles, dislocation loop transformation and irradiation-induced segregation were not investigated. Lu et al. performed positron annihilation spectroscopy to show that interstitial carbon atoms in equiatomic FeMnCoCrNi prevented the early formation of irradiation-induced damage at low doses (<1 dpa), but the later defect microstructural evolution still needs to be further studied [19,20].

Furthermore, the increase in the number of primary elements in MPEAs or HEAs is a mixed blessing for nuclear energy applications. It can reduce volumetric swelling but raise concern about irradiation hardening [9]. Therefore, when evaluating the effectiveness of a design strategy for improving radiation resistance, it is crucial to control the evolution of different types of defects, and balance the impacts to mechanical properties induced by these defects. In comparison to altering the number of principal elements in HEAs, here, we proposed a design strategy of adding interstitial carbon atoms to both efficiently reduce the irradiation hardening and volumetric swelling, and to decrease the extent of radiation-induced segregation (RIS) in HEAs. This strategy may provide a new pathway for designing HEAs with potential nuclear applications. It could also apply to refractory body-centered cubic HEAs, which is also considered for nuclear uses owing to their excellent high-temperature performance [21,22]. Recent studies have shown that large amounts of small interstitial atoms could be incorporated into body-centered cubic HEAs in the form of solid solution, which greatly improves the mechanical properties of metallic materials [23].

In this study, an interstitially alloyed HEA, $\text{Fe}_{49.5}\text{Mn}_{30}\text{Co}_{10}\text{Cr}_{10}\text{C}_{0.5}$ (at. %), was chosen to investigate the evolution of helium (He) bubbles, dislocation loops and RIS with increasing temperature under He ion irradiation. Moreover, as typical quaternary HEA and quinary HEA, $\text{Fe}_{50}\text{Mn}_{30}\text{Co}_{10}\text{Cr}_{10}$ and $\text{Fe}_{20}\text{Mn}_{20}\text{Co}_{20}\text{Cr}_{20}\text{Ni}_{20}$ Cantor alloy (hereafter called FeMnCoCrNi) were utilized as reference samples, respectively. The size distribution of He bubbles and dislocation loops were characterized by Cs-corrected scanning/transmission electron microscopy (S/TEM) to ensure the accuracy of the results. We also determined the elemental segregation of dislocation loops and He bubbles in three HEAs to reveal the underlying segregation mechanism. Additional nanoindentation studies were carried out to determine the irradiation hardening caused by the microstructure changes. Based on first-principles calculations, vacancy migration energies of different elements in HEAs were obtained, which reveals the elemental enrichment/depletion behavior around dislocation loops and He bubbles. Further, the local lattice distortion and charge transfer induced by interstitial carbon atoms were determined. Interstitial carbon atoms enhance the local lattice distortion and charge transfer in the alloy system due to its large variation in atomic size and electronegativity, and it can act as sinks to trap defects and inhibit defect evolution. The results are expected to offer a perspective on controlling the irradiation-induced changes in microstructures and

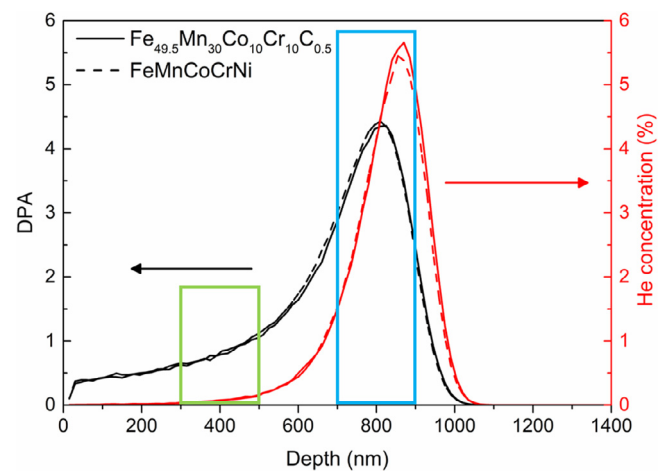


Fig. 1. The depth profiles of damage and implanted He concentration calculated using the SRIM-2013 software for $\text{Fe}_{49.5}\text{Mn}_{30}\text{Co}_{10}\text{Cr}_{10}\text{C}_{0.5}/\text{Fe}_{50}\text{Mn}_{30}\text{Co}_{10}\text{Cr}_{10}$ and FeMnCoCrNi irradiated with 400 keV He^+ ions at a fluence of 1×10^{17} ions/ cm^2 . The green box and the blue box represent the platform region and the peak region, respectively.

mechanical properties by tuning the concentration of interstitial carbon atoms in HEAs.

2. Materials and methodologies

2.1. Materials and irradiation

The alloys of interstitial HEA were prepared by arc-melting and casting in a vacuum induction furnace using pure metals and carbon with a nominal composition of $\text{Fe}_{49.5}\text{Mn}_{30}\text{Co}_{10}\text{Cr}_{10}\text{C}_{0.5}$ (at. %). The as-cast alloys were homogenized at 1200 °C for 2 h in an Ar atmosphere and then water-quenched. The as-homogenized bulk sample presented a single FCC structure [24]. $\text{Fe}_{20}\text{Mn}_{20}\text{Co}_{20}\text{Cr}_{20}\text{Ni}_{20}$ and $\text{Fe}_{50}\text{Mn}_{30}\text{Co}_{10}\text{Cr}_{10}$ HEAs were also prepared using the same processing method for comparison.

All samples before irradiation were mechanically polished using colloidal silica, then vibratory polished to remove the stress layer resulting in a mirror surface with a roughness of less than 3 nm. Subsequently, the samples were irradiated with 400 keV He^+ ions at a fluence of 1×10^{17} cm $^{-2}$ on the Xiamen Multiple Ion Beam at Xiamen University. The irradiation was performed at a temperature of 350 °C, 400 °C and 450 °C. The melting temperatures and homologous temperatures of these alloys [25,26] are shown in Table S1, and it can be seen that as their melting temperature are close, i.e., 1553 K and 1613 K for FeMnCoCrNi and $\text{Fe}_{50}\text{Mn}_{30}\text{Co}_{10}\text{Cr}_{10}/\text{Fe}_{49.5}\text{Mn}_{30}\text{Co}_{10}\text{Cr}_{10}\text{C}_{0.5}$, respectively, their homologous temperatures are almost equal. Therefore, it is reasonable to conduct comparative analysis at the same irradiation temperature. The damage profile and injected He concentration were calculated using SRIM-2013 in full cascade mode [27]. The input density of $\text{Fe}_{50}\text{Mn}_{30}\text{Co}_{10}\text{Cr}_{10}/\text{Fe}_{49.5}\text{Mn}_{30}\text{Co}_{10}\text{Cr}_{10}\text{C}_{0.5}$ and FeMnCoCrNi are 7.75 g/cm $^{-3}$ and 8.06 g/cm $^{-3}$, respectively. The displacement threshold energies were set to 40 eV for all the constituent elements [28]. The ion concentration and displacement per atom (dpa) as a function of the injected depth are shown in Fig. 1. The green box represents the platform region (about 300–500 nm), while the blue box represents the peak region (about 700–900 nm).

2.2. Materials characterization

The cross-sectional TEM samples were prepared by the focused-ion beam (FIB) lift-out technique on an FEI Scios Dual-Beam sys-

tem. The TEM samples were further “flashing polished”, an extremely short electrolytic polishing technology to entirely remove the FIB-induced artificial damage for reliable characterization and analysis [29]. Characterization of radiation-induced defects was carried out on an aberration-corrected STEM (FEI Themis Z) operating at 300 kV, equipped with a Super-X energy dispersive spectroscopy (EDS) with four windowless silicon-drift detectors. Spherical aberration correction was performed before each experiment to ensure 0.06 nm resolution under normal conditions. The dwell time was 2 μ s per pixel with a map size of 2048 \times 2048 pixels when acquiring EDS mapping, and each EDS mapping took roughly 30 min to reach a high signal-to-noise ratio. The statistical analysis of He bubbles and dislocation loops was based on several FIB samples using ImageJ software.

Nanoindentation tests were performed on samples before and after irradiation to obtain the behavior of irradiation hardening (G200 nanoindenter instrument, Agilent). A Berkovich-type indenter with 20 nm size was used to obtain the relationship between indentation depth and hardness using the continuous stiffness measurement (CSM) method. The maximum indentation depth was set at 1500 nm. The average hardness of each sample was calculated from ten indentation tests to avoid statistical errors.

2.3. First-principles calculations

The first-principles calculations of the $\text{Fe}_{49.5}\text{Mn}_{30}\text{Co}_{10}\text{Cr}_{10}\text{C}_{0.5}$ alloy were performed with the Vienna ab initio simulation package (VASP) using the projector-augmented wave (PAW) method [30]. The generalized gradient approximation with the Perdew-Burke-Ernzerhof (PBE) formulism was used to describe the exchange and correlation interactions [31]. Semi-core p-orbital electrons were considered for metal elements with 14, 13, 15, and 12 electrons used for Fe, Mn, Co and Cr, respectively. The studied system has a composition of $\text{Fe}_{49.5}\text{Mn}_{29.4}\text{Co}_{10.1}\text{Cr}_{10.1}\text{C}_{0.9}$ with one carbon atom included in the 3 \times 3 \times 3 supercell with a total of 109 atoms. The alloy system was constructed by the special quasi-random structure (SQS) method [32] to ensure the random arrangement of different types of atoms at the first and second-nearest neighbor sites. The Brillouin zone was sampled with a Monkhorst-Pack grid of 2 \times 2 \times 2. The energy cutoff of the plane wave was set to 500 eV and the force convergence criterion was set to 0.01 eV/ \AA . During all simulations, the spin polarization was considered. For the calculation of the lattice distortion, the results were averaged over three structures with the carbon atom placed at different interstitial sites. The octahedral site is the stable interstitial site for the carbon atom based on relaxed structures. For each configuration, three different initial paramagnetic spin moments were considered and the relaxed configuration with the lowest system energy was selected. For comparison, the lattice distortion of equiatomic FeMnCoCrNi and $\text{Fe}_{50.0}\text{Mn}_{29.6}\text{Co}_{10.2}\text{Cr}_{10.2}$ was also calculated with the same simulation settings. The vacancy migration energies were calculated using the climbing-image nudged elastic band (CI-NEB) [33] method with one intermediate image and a force convergence criterion of 0.03 eV/ \AA . First, ten randomly selected migration paths between nearest neighbor sites were calculated for each type of migration atom. Next, different migration paths near the interstitial carbon atom were selected to study the impact of carbon atoms on the migration barriers. The choice of the 3 \times 3 \times 3 supercell (108 atoms) was further validated by the comparison with a supercell size of 4 \times 4 \times 4 (256 atoms), showing that the difference in vacancy migration energy only differs by ~9.3 % and is relatively small (see the comparison results in **Supplementary materials Method**). The Bader charge analysis was performed to determine the charge transfer of each type of atom [34].

3. Results

3.1. He bubbles distribution

The cross-sectional distribution of He bubbles along the depth for all materials under different irradiation conditions is shown in Fig. S1, taken by TEM bright-field (BF) under defocus condition. Fig. 2 shows the He bubble densities in $\text{Fe}_{49.5}\text{Mn}_{30}\text{Co}_{10}\text{Cr}_{10}\text{C}_{0.5}$, $\text{Fe}_{50}\text{Mn}_{30}\text{Co}_{10}\text{Cr}_{10}$, and FeMnCoCrNi as a function of implanted depth irradiated at 350 °C, 400 °C, 450 °C. In general, the He bubble density distributions in the three alloys agree with the SRIM calculations and have a similar profile with a significant increase at ~500 nm and a peak at 850 nm. Moreover, as the temperature increases, the He bubble peak gradually shifts to a deeper region. As a result, the analysis of He bubble focused on two regions, the platform region (~300–500 nm) with a low density of He and the peak region (~800–900 nm) with a high density He atoms.

Bright-field images were taken under the defocused condition in Fig. 3, showing the He bubble distribution of the three alloys in the platform region after He irradiation at a fluence of $1 \times 10^{17} \text{ cm}^{-2}$ at 350 °C, 400 °C, 450 °C, respectively. The irradiation temperature strongly influences the size and density of He bubbles. The higher temperature will promote the diffusion of He atoms and the agglomeration of He bubbles. Fig. 4 depicts the variation of He bubble size and density with increasing temperature in the platform region. It reveals that the evolution of bubbles follows a typical temperature pattern, i.e., as the temperature increases, the size grows while the density decreases. The He bubble size in $\text{Fe}_{49.5}\text{Mn}_{30}\text{Co}_{10}\text{Cr}_{10}\text{C}_{0.5}$ is smaller than $\text{Fe}_{50}\text{Mn}_{30}\text{Co}_{10}\text{Cr}_{10}$ and even FeMnCoCrNi in the platform region. With the increase of irradiation temperature, the trend is more pronounced. Additionally, the density of He bubbles in $\text{Fe}_{49.5}\text{Mn}_{30}\text{Co}_{10}\text{Cr}_{10}\text{C}_{0.5}$ is slightly higher than $\text{Fe}_{50}\text{Mn}_{30}\text{Co}_{10}\text{Cr}_{10}$, but much lower than FeMnCoCrNi . The distribution of the He bubble size at different temperatures for the three alloys is shown in Fig. 5. With increasing temperature, the size distributions of He bubbles become wider in all alloys. $\text{Fe}_{50}\text{Mn}_{30}\text{Co}_{10}\text{Cr}_{10}$ has the widest He bubbles size distribution at the same irradiation temperature, whereas $\text{Fe}_{49.5}\text{Mn}_{30}\text{Co}_{10}\text{Cr}_{10}\text{C}_{0.5}$ has the narrowest, and the disparity is accentuated as the irradiation temperature increases.

Similarly, we analyzed the distribution of He bubbles in the peak region for the three alloys at various temperatures, as shown in Figs. 6 and 7. The variability in size and density is similar to those found in the platform region, but the density is higher, and the size distribution appears to be more uniform. The He bubble size in the peak region is less than that in the platform region, and the growth is relatively slower with increasing irradiation temperature. Nevertheless, $\text{Fe}_{50}\text{Mn}_{30}\text{Co}_{10}\text{Cr}_{10}$ has the largest He bubbles size in the peak region at 450 °C. Table 1 summarizes the He bubble volumetric swelling of the three alloys in the platform and peak regions at different temperatures. It can be observed that $\text{Fe}_{49.5}\text{Mn}_{30}\text{Co}_{10}\text{Cr}_{10}\text{C}_{0.5}$ exhibits the lowest volumetric swelling in both the platform and peak regions, while $\text{Fe}_{50}\text{Mn}_{30}\text{Co}_{10}\text{Cr}_{10}$ has the highest volumetric swelling.

3.2. Dislocation loop evolution

The dislocation loops in three alloys were characterized using the on-zone STEM-BF method. This characterization method improves counting precision since it can simultaneously obtain all \mathbf{g} vectors and detect all dislocation loops simultaneously. Fig. 8 shows the typical on-zone STEM-BF images of the dislocation loops formed in the platform region at a depth of 300–500 nm (about 1 dpa) for $\text{Fe}_{49.5}\text{Mn}_{30}\text{Co}_{10}\text{Cr}_{10}\text{C}_{0.5}$, $\text{Fe}_{50}\text{Mn}_{30}\text{Co}_{10}\text{Cr}_{10}$, and FeMnCoCrNi irradiated at 350 °C, 400 °C and 450 °C, respectively. The images were taken under the [110] zone axis. Irradiation-

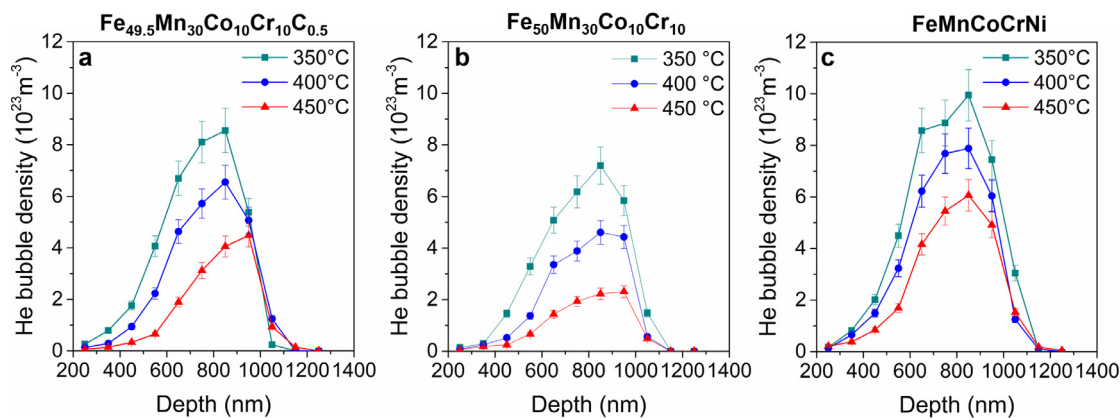


Fig. 2. The density of He bubbles along the irradiation depth at different irradiation temperatures (350 °C, 400 °C and 450 °C) for (a) Fe_{49.5}Mn₃₀Co₁₀Cr₁₀C_{0.5}, (b) Fe₅₀Mn₃₀Co₁₀Cr₁₀, and (c) FeMnCoCrNi, respectively.

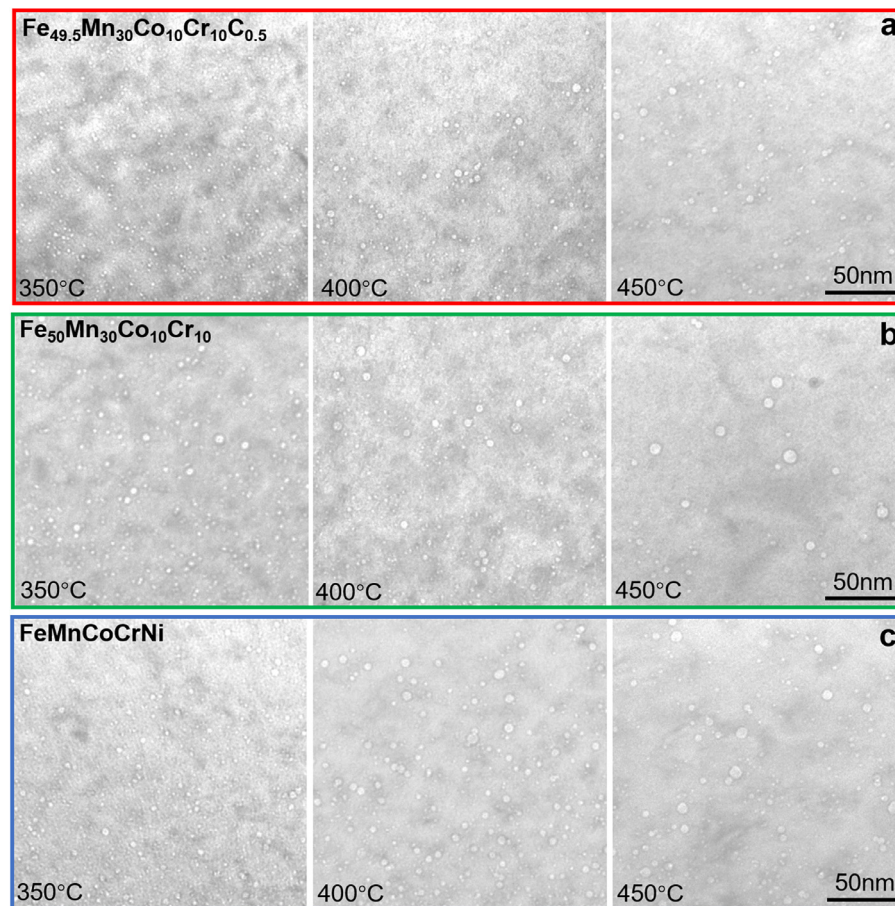


Fig. 3. Comparison of He bubble distribution in the platform region with TEM bright-field under-focused condition at 350 °C, 400 °C and 450 °C for (a) Fe_{49.5}Mn₃₀Co₁₀Cr₁₀C_{0.5}, (b) Fe₅₀Mn₃₀Co₁₀Cr₁₀ and (c) FeMnCoCrNi, respectively.

Table 1

Volumetric swelling of Fe₅₀Mn₃₀Co₁₀Cr₁₀, FeMnCoCrNi and Fe_{49.5}Mn₃₀Co₁₀Cr₁₀C_{0.5} in the platform region and peak region at an irradiation temperature of 350 °C, 400 °C and 450 °C.

Volumetric swelling (%)	Platform region			Peak region		
	350 °C	400 °C	450 °C	350 °C	400 °C	450 °C
Fe ₅₀ Mn ₃₀ Co ₁₀ Cr ₁₀	0.035	0.052	0.090	0.25	0.63	1.50
FeMnCoCrNi	0.029	0.040	0.080	0.089	0.11	0.19
Fe _{49.5} Mn ₃₀ Co ₁₀ Cr ₁₀ C _{0.5}	0.014	0.022	0.028	0.076	0.10	0.15

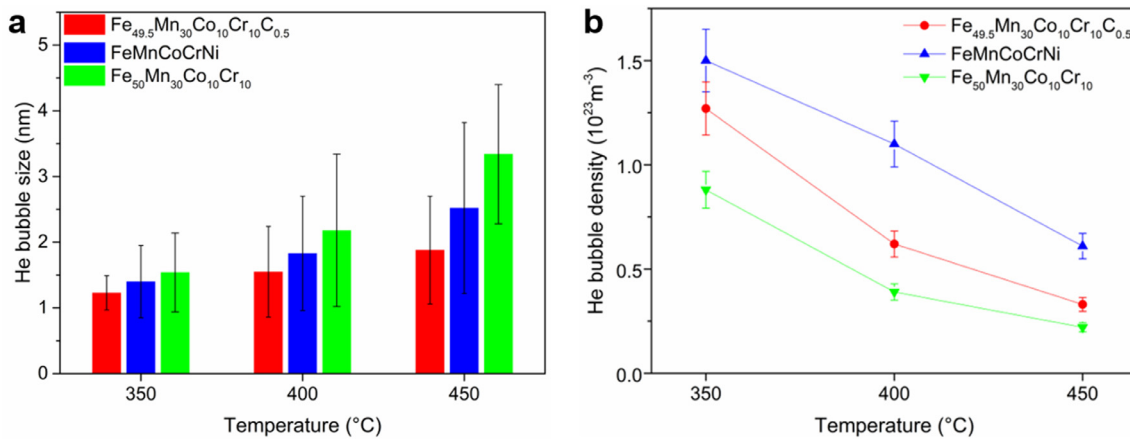


Fig. 4. The distribution of the (a) average size and (b) average density of He bubbles in the platform region for $\text{Fe}_{49.5}\text{Mn}_{30}\text{Co}_{10}\text{Cr}_{10}\text{C}_{0.5}$, FeMnCoCrNi and $\text{Fe}_{50}\text{Mn}_{30}\text{Co}_{10}\text{Cr}_{10}$, at 350 °C, 400 °C and 450 °C, respectively.

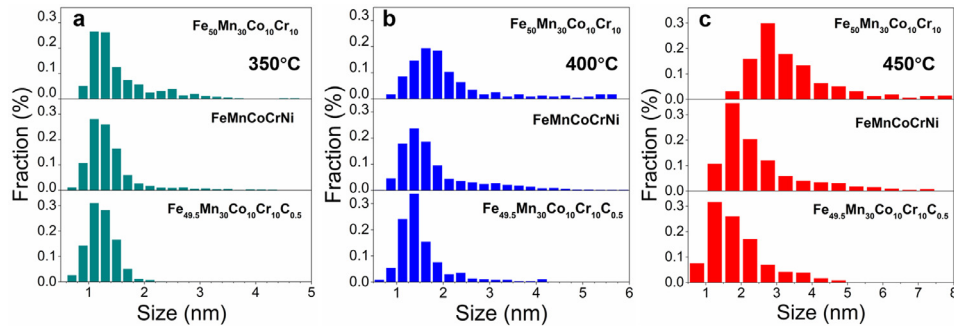


Fig. 5. Statistical distribution of the He bubble size in the platform region for $\text{Fe}_{49.5}\text{Mn}_{30}\text{Co}_{10}\text{Cr}_{10}\text{C}_{0.5}$, FeMnCoCrNi and $\text{Fe}_{50}\text{Mn}_{30}\text{Co}_{10}\text{Cr}_{10}$, at (a) 350 °C, (b) 400 °C and (c) 450 °C, respectively.

induced dislocation loops in FCC high entropy alloys are classified into 1/3 <111> faulted loops and 1/2 <110> perfect loops, which are marked by blue arrows and red arrows in Fig. 8, respectively. The size and density of the dislocation loop change dramatically with increasing temperature.

Fig. 9a–c present the distribution of dislocation loops size for the three alloys irradiated to about 1 dpa at 350 °C, 400 °C and 450 °C. $\text{Fe}_{49.5}\text{Mn}_{30}\text{Co}_{10}\text{Cr}_{10}\text{C}_{0.5}$ has a relatively higher fraction of larger dislocation loops, while FeMnCoCrNi has the highest fraction of smaller dislocation loops. In general, as shown in Fig. 9d, the loop density in $\text{Fe}_{49.5}\text{Mn}_{30}\text{Co}_{10}\text{Cr}_{10}\text{C}_{0.5}$ was found to be lower than that in FeMnCoCrNi and $\text{Fe}_{50}\text{Mn}_{30}\text{Co}_{10}\text{Cr}_{10}$, with the difference becoming smaller as the temperature increases. A rapid increase in the size and a decrease in the density of the dislocated loops with increasing temperature were observed in all materials. It means that a fraction of small dislocation loops interacts with each other and form larger dislocation loops. Moreover, Fig. 9e shows the fraction of two types of loops in three materials at the studied temperatures. $\text{Fe}_{49.5}\text{Mn}_{30}\text{Co}_{10}\text{Cr}_{10}\text{C}_{0.5}$ has the lowest percentage of faulted loop, while FeMnCoCrNi has the highest. With increasing temperature, the fraction of faulted loops decreases from 71% to 33%, 79% to 46% and 89% to 63% in $\text{Fe}_{49.5}\text{Mn}_{30}\text{Co}_{10}\text{Cr}_{10}\text{C}_{0.5}$, $\text{Fe}_{50}\text{Mn}_{30}\text{Co}_{10}\text{Cr}_{10}$ and FeMnCoCrNi, respectively. Therefore, increasing irradiation temperature can effectively promote the growth of dislocation loops [35,36].

3.3. Radiation-induced segregation at dislocation loops and He bubbles

The irradiation-induced segregation at dislocation loops and He bubbles was examined using advanced aberration-corrected STEM-

EDS equipment. Fig. 10 represents a STEM-HAADF image of an edge-on dislocation loop in $\text{Fe}_{49.5}\text{Mn}_{30}\text{Co}_{10}\text{Cr}_{10}\text{C}_{0.5}$ irradiated at 350 °C. The T sign was used to indicate the inserted half-atomic planes, as shown in Fig. 10b. It shows that the dislocation loop is an interstitial 1/3 <111> faulted loop and is parallel to the STEM electron beam direction. The region in the blue box was analyzed through high-resolution EDS acquisition to improve spatial resolution. Fig. 11a shows the distribution of elements around the faulted loops. We observed that Fe and Co tend to be enriched around the center of the loop, while Cr and Mn tend to be depleted. There is no observable segregation of interstitial carbon atoms.

RIS characterizations were performed for the other alloys in a similar manner. For each alloy, at least three dislocation loops were analyzed to reduce the statistical variation and ensure the consistency of the results. The composition profiles across dislocation loops of $\text{Fe}_{49.5}\text{Mn}_{30}\text{Co}_{10}\text{Cr}_{10}\text{C}_{0.5}$, $\text{Fe}_{50}\text{Mn}_{30}\text{Co}_{10}\text{Cr}_{10}$, and FeMnCoCrNi from EDS mapping are compared in Fig. 11a–c, respectively. The quantitative analysis of low carbon concentration measured by EDS is problematic, and therefore the profiles are not plotted. The segregation of elements does not always vary monotonically, such as Fe in $\text{Fe}_{49.5}\text{Mn}_{30}\text{Co}_{10}\text{Cr}_{10}\text{C}_{0.5}$, where it starts with a gradual increase in concentration from the matrix to the dislocation loop, followed by a decrease around the dislocation loop (<1 nm). This can be attributed to multiple competing mechanisms, on which a more in-depth discussion will be provided later. In addition, the results of compositional concentration variation across the dislocation loop at 350 °C are summarized in Fig. 11d. The lowest level of RIS is found in $\text{Fe}_{49.5}\text{Mn}_{30}\text{Co}_{10}\text{Cr}_{10}\text{C}_{0.5}$, whereas the maximum level is found in $\text{Fe}_{50}\text{Mn}_{30}\text{Co}_{10}\text{Cr}_{10}$.

We also utilized a similar strategy to characterize the RIS behavior near He bubbles. As shown in Fig. 12a, the darker areas

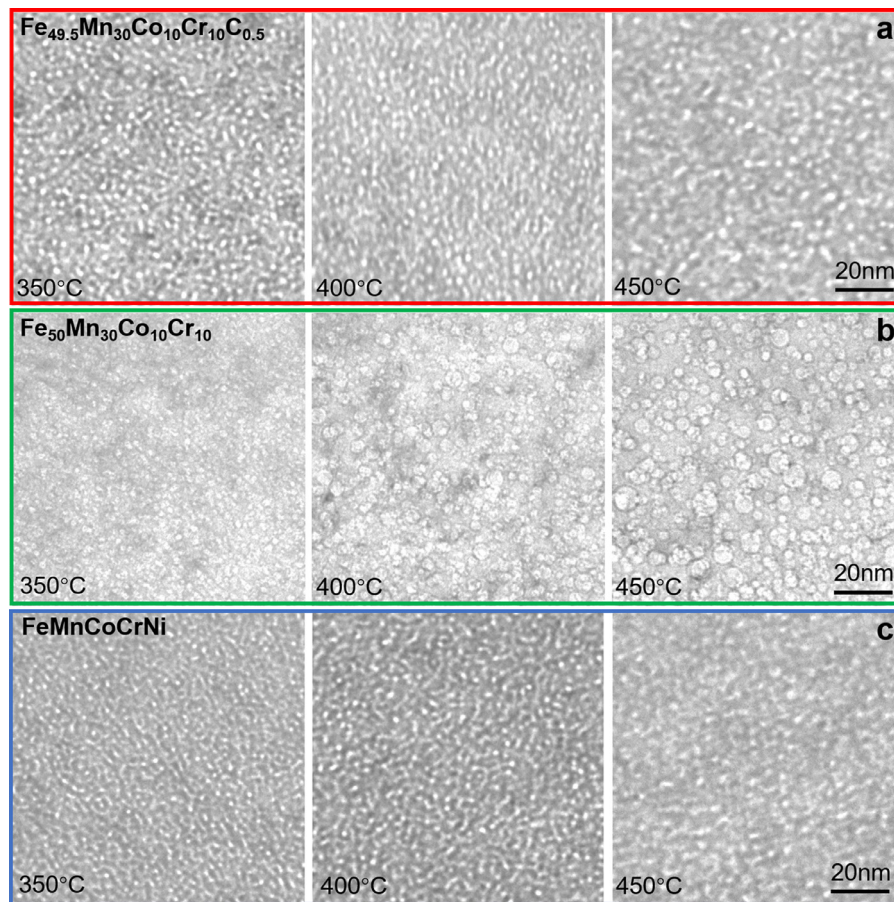


Fig. 6. Comparison of the He bubble distribution in the peak region under TEM bright-field under-focused condition at 350 °C, 400 °C and 450 °C for (a) $\text{Fe}_{49.5}\text{Mn}_{30}\text{Co}_{10}\text{Cr}_{10}\text{C}_{0.5}$, (b) $\text{Fe}_{50}\text{Mn}_{30}\text{Co}_{10}\text{Cr}_{10}$ and (c) FeMnCoCrNi , respectively.

in the HAADF image represent He bubbles due to the lower mass contrast. STEM-EDS mapping shows that the surface of the He bubble exhibits the same segregation behavior as the faulted dislocation loop, with enrichment in Fe and Co and depletion in Mn and Cr, as shown in Fig. 12b.

3.4. Radiation-induced hardening

The change of the mechanical properties induced by irradiation-induced defects can be reflected via nanoindentation testing. The discrete data points before 150 nm depth were discarded in this investigation to prevent influence from indentation size and surface roughness. Further, Nix and Gao's method was used to determine the hardness of unirradiated and irradiated samples [37]. The relationship between the variation of nanohardness and indentation depth can be expressed as follows:

$$H = H_0 \sqrt{1 + \frac{h^*}{h}}, \quad (1)$$

where H is the hardness at the indentation depth of h , h^* is a characteristic length associated with the indenter and material type, and H_0 is the hardness at infinite depth.

The relationship between the average nanohardness and indentation depth before and after irradiation for the three alloy samples is shown in Fig. 13a–c. According to Eq. (1), H^2 has a good linear relationship with $1/h$. As a result, the irradiation hardness can be described by determining the inflection points of their bilinearities, which is at a depth of about 250 nm in all cases of this study. Therefore, the hardness value at this position was calculated and converted to hardening for better comparison, as shown

in Fig. 13d. $\text{Fe}_{49.5}\text{Mn}_{30}\text{Co}_{10}\text{Cr}_{10}\text{C}_{0.5}$ has the lowest irradiation hardening, while FeMnCoCrNi has the highest irradiation hardening.

4. Discussion

4.1. The role of interstitial carbon atoms on the evolution of He bubble

A large amount of He can be generated by transmutation during the neutron radiation, which accumulates easily in the metallic material and causes performance degradation. Therefore, it is crucial to reduce the size of He bubbles in nuclear structural materials. Previous studies tended to utilize dispersed precipitates or introduce high-density grain boundaries as traps to disperse helium atoms to suppress the growth of helium bubbles [38,39]. Chen et al. found that the size of He bubbles at high temperature was smaller in NiCoFeCr high-entropy alloys than pure Ni, since more significant lattice distortion and chemical disorder can inhibit the diffusion and growth of He bubbles [40]. Further, they introduced minor alloying elements (Al/Cu/Ti) into NiCoFeCr, which instead promoted the diffusion and growth of He bubble because the vacancy migration energy was reduced [41].

As shown in Figs. 4 and 7, for $\text{Fe}_{49.5}\text{Mn}_{30}\text{Co}_{10}\text{Cr}_{10}\text{C}_{0.5}$, the He bubble size is remarkably smaller than that of the quaternary $\text{Fe}_{50}\text{Mn}_{30}\text{Co}_{10}\text{Cr}_{10}$ high-entropy alloys, and even smaller than that of the quinary FeMnCoCrNi high-entropy alloys. Meanwhile, the trend of He bubble density changes in the opposite way. The peak region (800–900 nm) has the highest density of He bubbles, since most of the injected He atoms are clustered in this region. How-

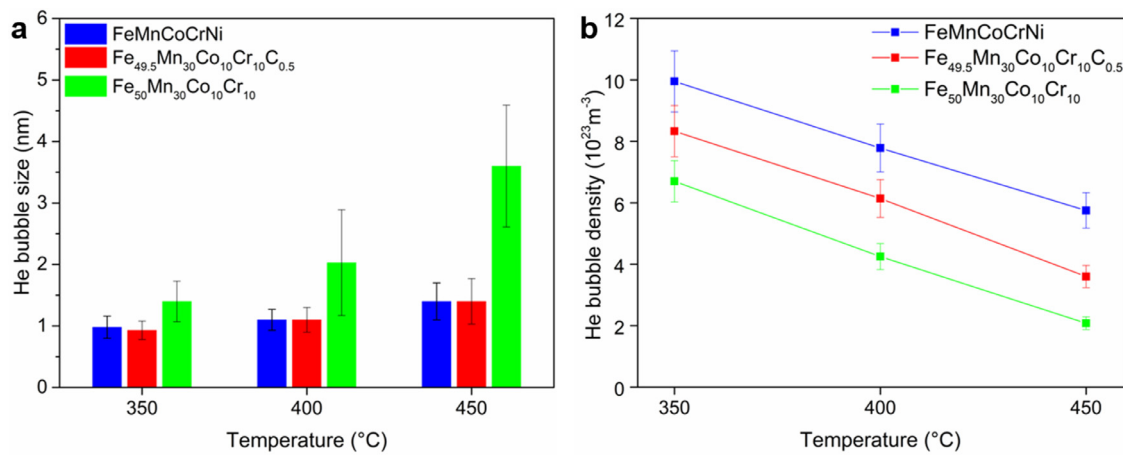


Fig. 7. The distribution of the (a) average size and (b) average density of He bubbles in the peak region for Fe_{49.5}Mn₃₀Co₁₀Cr₁₀C_{0.5}, FeMnCoCrNi and Fe₅₀Mn₃₀Co₁₀Cr₁₀ at 350 °C, 400 °C and 450 °C, respectively.

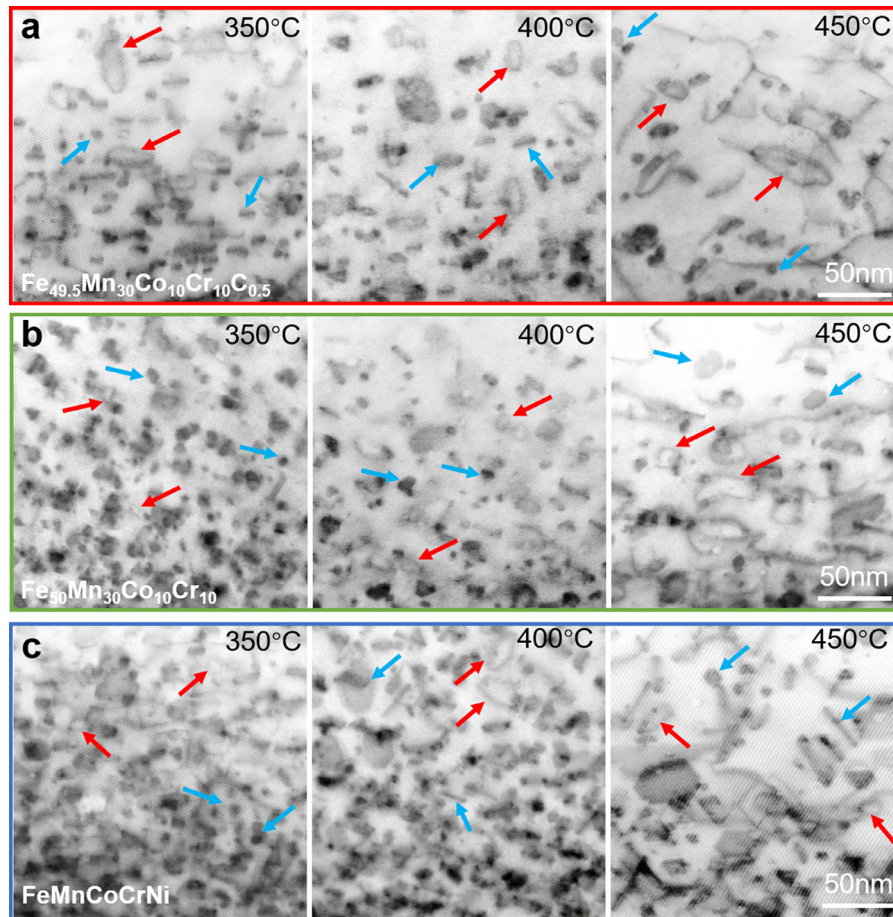


Fig. 8. On [110] zone STEM-BF images of (a) Fe_{49.5}Mn₃₀Co₁₀Cr₁₀C_{0.5}, (b) Fe₅₀Mn₃₀Co₁₀Cr₁₀ and (c) FeMnCoCrNi at a dose of 1 dpa at 350 °C, 400 °C and 450 °C, respectively. The blue arrows represent the typical a/3<111> dislocation loops, and the red arrows represent the typical a/2<110> dislocation loops.

ever, larger He bubble sizes are not always associated with higher He concentrations. In fact, the size of He bubbles is also closely related to the nucleation density. It increases with increasing He concentration only if the nucleation density remains essentially stable. The high-density small interstitial clusters in the peak region permit it to act as nucleation sites for He bubbles, preventing rapid bubble growth. Therefore, this may also explain the smaller size of He bubbles in the peak region compared to the platform region

and the moderate growth of He bubbles in the peak region with the increase of temperature. In addition, in comparison with FeMnCoCrNi, Fe_{49.5}Mn₃₀Co₁₀Cr₁₀C_{0.5} exhibits both a lower density and a smaller size of He bubbles. There may be two reasons for this. On the one hand, a fraction of He atoms tend to form extremely small He bubble so that they are undetected by the bright-field TEM mode in Fe_{49.5}Mn₃₀Co₁₀Cr₁₀C_{0.5}. On the other hand, the bubbles in Fe_{49.5}Mn₃₀Co₁₀Cr₁₀C_{0.5} could have higher He atoms den-

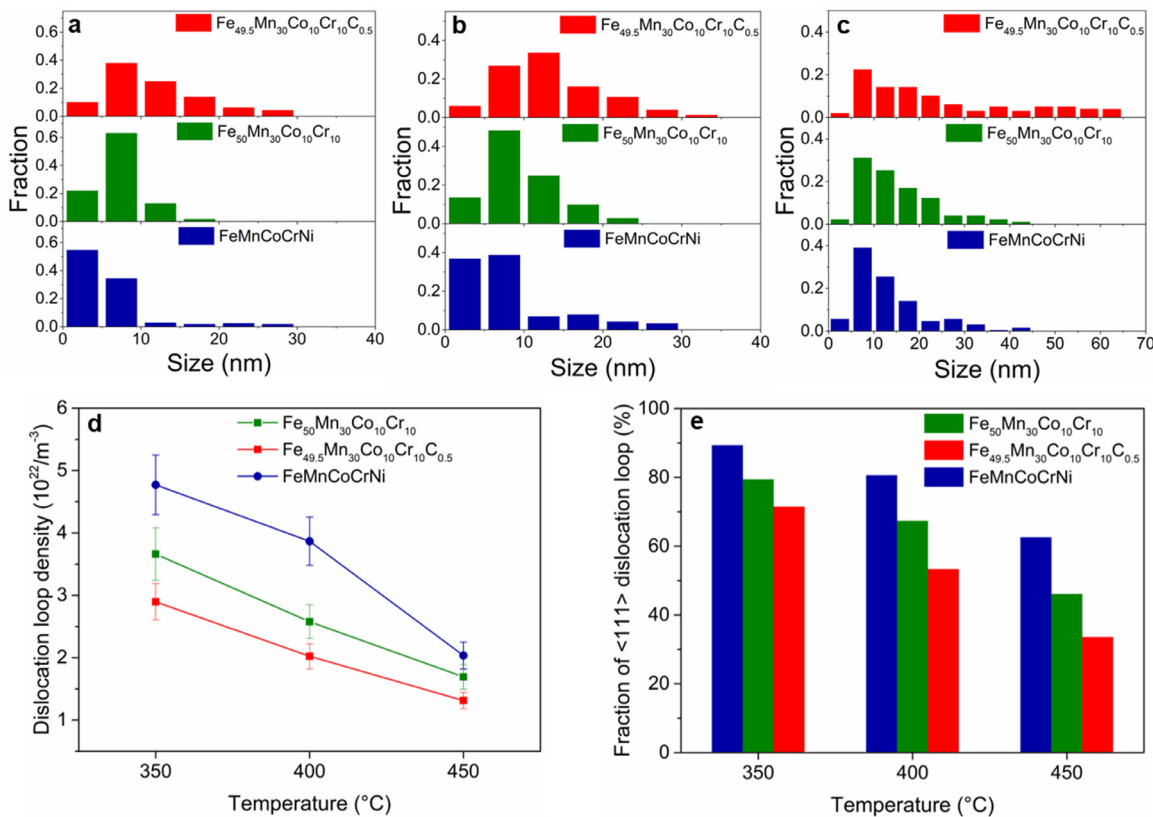


Fig. 9. The distribution of the (a)–(c) dislocation loop size, (d) average dislocation loop density and (e) the fraction of $a/3<111>$ dislocation loop in the platform region for $\text{Fe}_{49.5}\text{Mn}_{30}\text{Co}_{10}\text{Cr}_{10}\text{C}_{0.5}$, FeMnCoCrNi and $\text{Fe}_{50}\text{Mn}_{30}\text{Co}_{10}\text{Cr}_{10}$ at 350 °C, 400 °C and 450 °C, respectively.

sity than that in FeMnCoCrNi [42]. A similar work shows that the density of He atoms in He bubbles increases significantly with the increase of Fe content in NiFe alloys [43,44], because the higher Fe concentration stabilizes the stacking fault structure, which inhibits the evolution of dislocation network around He bubbles and the emission of dislocation, resulting in a higher He atom density in the bubble. The aforementioned reasons could explain the phenomenon of both lower density and smaller size of He bubbles in $\text{Fe}_{49.5}\text{Mn}_{30}\text{Co}_{10}\text{Cr}_{10}\text{C}_{0.5}$.

The volumetric swelling behaviors of the three alloys at different temperatures are compared in Table 1. It is found that $\text{Fe}_{49.5}\text{Mn}_{30}\text{Co}_{10}\text{Cr}_{10}\text{C}_{0.5}$ has the best volumetric swelling resistance. It has been shown that carbon atoms tend to combine with vacancies to create carbon-vacancy complexes in Fe-based alloys, raising the migration energy and limiting the vacancy clustering [45]. Our first-principles calculations also showed that, in $\text{Fe}_{49.5}\text{Mn}_{30}\text{Co}_{10}\text{Cr}_{10}\text{C}_{0.5}$, the vacancy migration energy increases significantly when vacancies jump between the first nearest neighbors around the interstitial carbon atoms, as marked in Fig. 14a (e.g., from 0.99 to 1.8 eV for a Mn atom). Moreover, we found that interstitial carbon atoms prefer to trap vacancies due to the lower migration energy required for vacancies to move towards interstitial atoms compared to moving away from them, as shown in Fig. 14b. According to the previous study [41,46], the diffusion of He is driven by the replacement mechanism at 0.2–0.5 T_m:

$$D_{\text{He}} \cong D_V (\text{replacement mechanism}), \quad (2)$$

where the effective He diffusivity (D_{He}) is mainly dominated by the vacancy diffusivity (D_V). This is because the He atoms are replaced by self-interstitial atoms and diffuse interstitially until they are recaptured by another vacancy. Therefore, the vacancy migration energy plays an essential role on the diffusion and evolution

of He bubble. It indicates that interstitial carbon atoms effectively delayed vacancy diffusion to inhibit He bubble growth.

The small-size interstitial carbon atoms prefer to occupy octahedral interstitial sites in the studied alloy, which induces more significant local lattice distortion compared to those induced by principal elements due to remarkable size variation between the interstitial carbon atoms and principal elements. Based on first-principles calculations, the local lattice distortion in HEAs can be described quantitatively as follows:

$$\Delta d = \frac{1}{N} \sum \sqrt{(x_i - x'_i)^2 + (y_i - y'_i)^2 + (z_i - z'_i)^2}, \quad (3)$$

where x_i , y_i , z_i and x'_i , y'_i , z'_i represent the coordinates of atom i before and after structure relaxation, respectively. The local lattice distortion of $\text{Fe}_{49.5}\text{Mn}_{30}\text{Co}_{10}\text{Cr}_{10}\text{C}_{0.5}$, FeMnCoCrNi and $\text{Fe}_{50}\text{Mn}_{30}\text{Co}_{10}\text{Cr}_{10}$ are 0.0421 Å, 0.0418 Å and 0.0356 Å, respectively. Therefore, the average lattice distortion induced by small interstitial carbon atoms ($\text{Fe}_{49.5}\text{Mn}_{30}\text{Co}_{10}\text{Cr}_{10}\text{C}_{0.5}$) is stronger than the quaternary alloy without carbon ($\text{Fe}_{50}\text{Mn}_{30}\text{Co}_{10}\text{Cr}_{10}$) and is approximately equal to the quinary alloy of FeMnCoCrNi . In addition, the fluctuation range of atomic bond distances is also an important characteristics of local lattice distortion, with wider fluctuations often implying stronger lattice distortion [47,48]. The distributions of bond distances in the $\text{Fe}_{50}\text{Mn}_{30}\text{Co}_{10}\text{Cr}_{10}$, $\text{Fe}_{49.5}\text{Mn}_{30}\text{Co}_{10}\text{Cr}_{10}\text{C}_{0.5}$ and FeMnCoCrNi are shown in Fig. 15. It is found that $\text{Fe}_{49.5}\text{Mn}_{30}\text{Co}_{10}\text{Cr}_{10}\text{C}_{0.5}$ has the broadest distribution with extreme values approaching 8%, which is mainly due to the large local atomic displacement around interstitial carbon atoms. In addition, the electronegativity of the interstitial carbon atom is also significantly higher than that of the principal elements in $\text{Fe}_{49.5}\text{Mn}_{30}\text{Co}_{10}\text{Cr}_{10}\text{C}_{0.5}$. According to Bader charge analysis, the standard deviation of charge transfer is 0.270 in $\text{Fe}_{50}\text{Mn}_{30}\text{Co}_{10}\text{Cr}_{10}$ and 0.294 in $\text{Fe}_{49.5}\text{Mn}_{30}\text{Co}_{10}\text{Cr}_{10}\text{C}_{0.5}$, suggesting that the addition

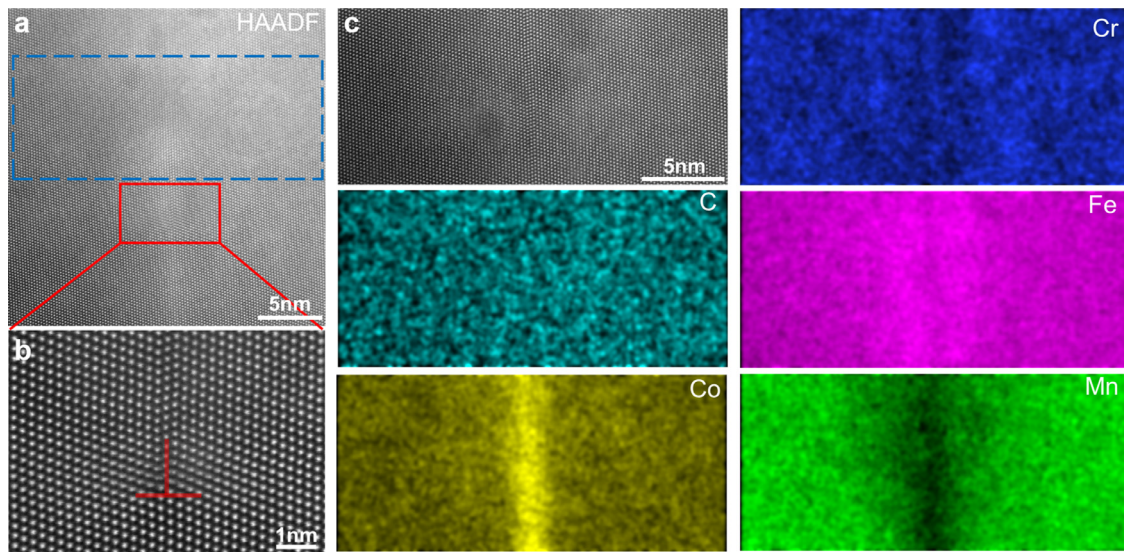


Fig. 10. Radiation-induced segregation near a dislocation loop in $\text{Fe}_{49.5}\text{Mn}_{30}\text{Co}_{10}\text{Cr}_{10}\text{C}_{0.5}$ at an irradiation temperature of 350 °C. (a) STEM-HAADF image of a dislocation loop; (b) high-resolution HAADF image indicates the interstitial type of the dislocation loop shown in (a); (c) The dislocation loop in the selected blue region of (a) and the corresponding EDS mapping.

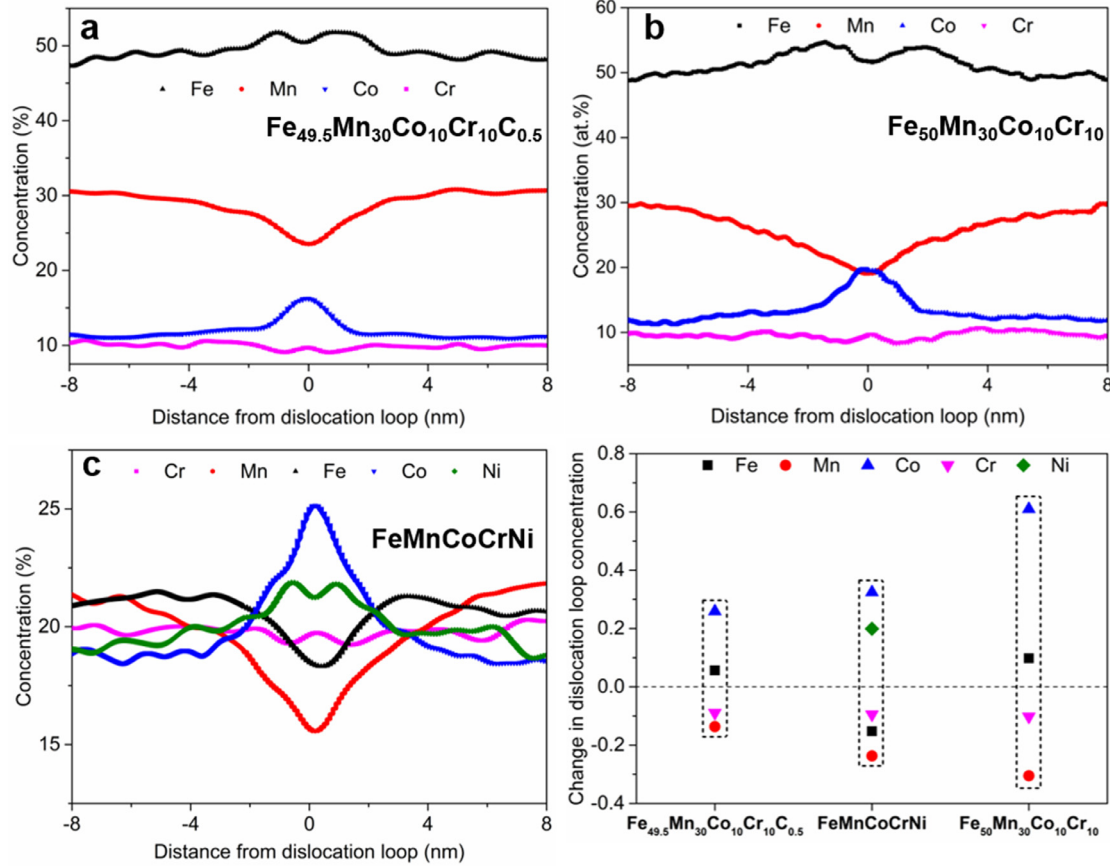


Fig. 11. Composition profiles around the dislocation loops at an irradiation temperature of 350 °C in (a) $\text{Fe}_{49.5}\text{Mn}_{30}\text{Co}_{10}\text{Cr}_{10}\text{C}_{0.5}$, (b) $\text{Fe}_{50}\text{Mn}_{30}\text{Co}_{10}\text{Cr}_{10}$ and (c) FeMnCoCrNi . (d) Comparison of the relative change in elemental composition between the dislocation loop and matrix.

of trace interstitial carbon atoms causes an increase in the fluctuation of charge transfer. The larger difference in charge transfer usually leads to an increase in local lattice distortion [49] and increase in the local atomic-level pressure [50] which can further impact the defect formation energies and migration behaviors [51].

Moreover, according to experiments, the $\text{Fe}_{49.5}\text{Mn}_{30}\text{Co}_{10}\text{Cr}_{10}\text{C}_{0.5}$ has the narrowest He bubble size distribution with less amount of

large helium bubbles, while $\text{Fe}_{50}\text{Mn}_{30}\text{Co}_{10}\text{Cr}_{10}$ has the broadest He bubble size distribution, as shown in Fig. 5. This difference in size distribution is also shown to be closely related to the efficiency of defect recombination, where stronger defect recombination, corresponding to smaller difference in mobility between vacancy and interstitial atoms, promotes more uniform He bubble growth [52].

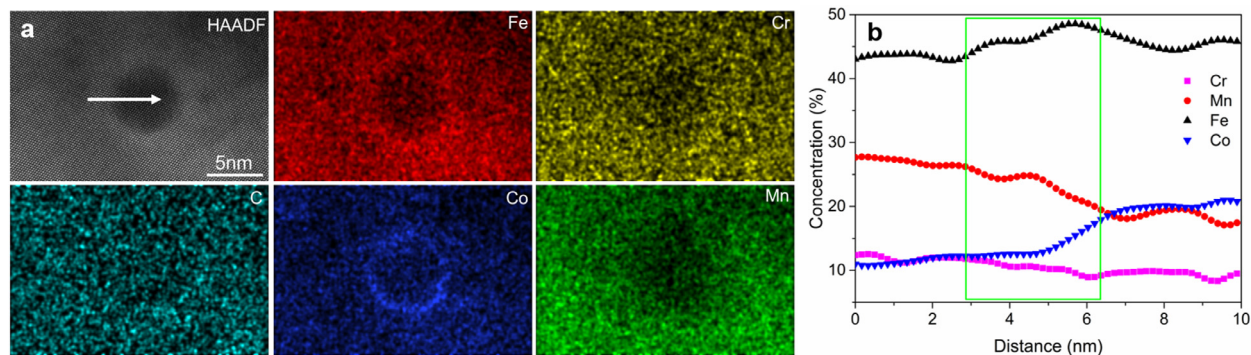


Fig. 12. (a) RIS near a He bubble in $\text{Fe}_{49.5}\text{Mn}_{30}\text{Co}_{10}\text{Cr}_{10}\text{C}_{0.5}$ at an irradiation temperature of 450 °C. (b) The composition profile along the white arrow in (a), where the green box corresponds to the surface of the He bubble.

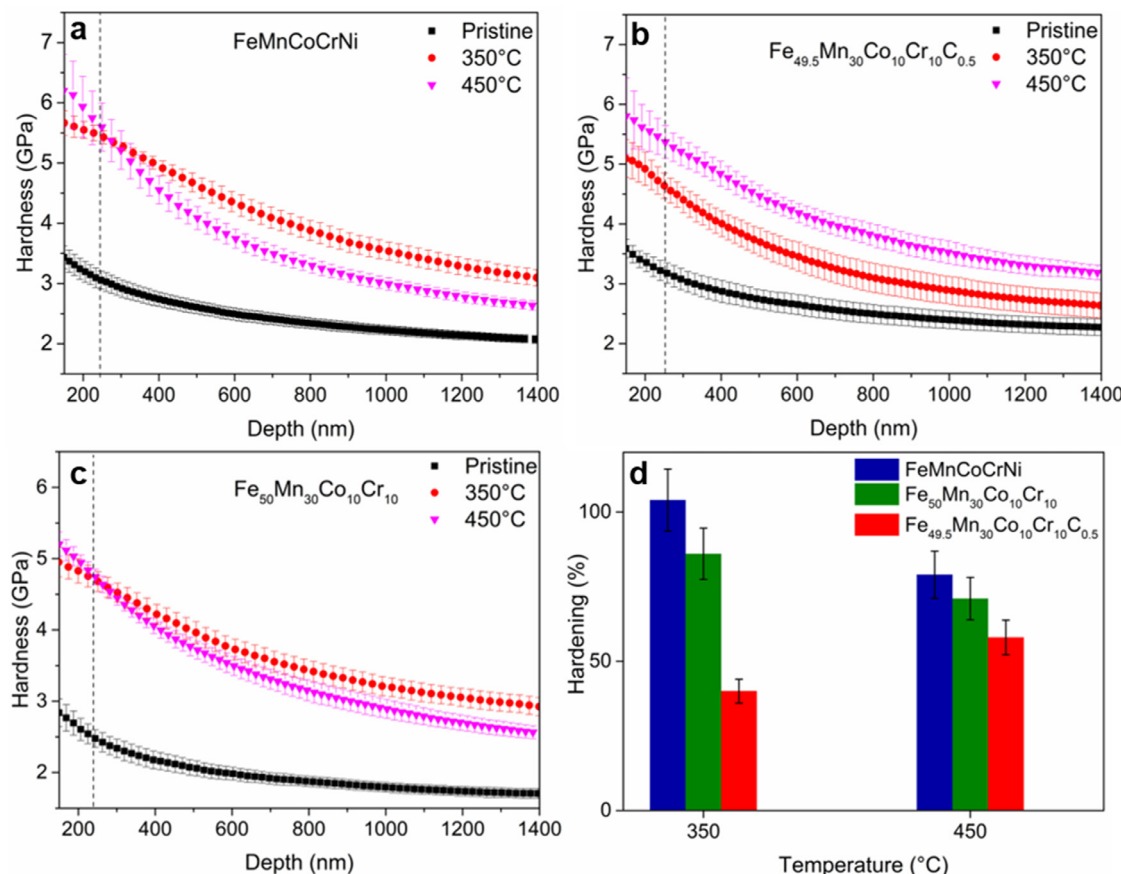


Fig. 13. Average nanohardness as a function of the indentation depth of (a) FeMnCoCrNi , (b) $\text{Fe}_{49.5}\text{Mn}_{30}\text{Co}_{10}\text{Cr}_{10}\text{C}_{0.5}$ and (c) $\text{Fe}_{50}\text{Mn}_{30}\text{Co}_{10}\text{Cr}_{10}$ for the pristine sample and irradiated samples at 350 °C and 450 °C. (d) Comparison of irradiation hardening for the three alloys at an irradiation temperature of 350 °C and 450 °C.

In conclusion, we show that interstitial carbon atoms can suppress volumetric swelling more effectively than increasing the number of principal elements. The more critical aspect is that it inhibited the vacancy migration and enhanced local lattice distortion, thus delaying the growth rate of He bubbles and reducing volumetric swelling.

4.2. The effect of interstitial carbon atoms on the dislocation loop evolution

Irradiation-induced interstitial atoms surviving from the recombination process typically form dislocation loops in FCC materials, and these dislocation loops can further grow by absorbing moving interstitial atoms. The dislocation loops are generally divided into

1/3 <111> type and 1/2 <110> type, which were both observed in this study using on-zone STEM-BF mode. With increasing irradiation temperature, the mobility of interstitial atoms increases, thus promoting the transformation of faulted loops into perfect loops according to the known reaction [53]:

$$(a/3)\langle 111 \rangle + (a/6)\langle 112 \rangle = a/2\langle 110 \rangle, \quad (4)$$

this process of transformation with increasing temperature can be seen in Figs. 8 and 9. As the irradiation temperature increases, the number of dislocation loops decreases and their size grows in all three alloys, and in addition, the fraction of faulted loops decreases due to the transformation into perfect loops. The formation of large dislocation loops with lower density is mainly due to the dissolution of tiny defect clusters at high temperature [36], which reduces

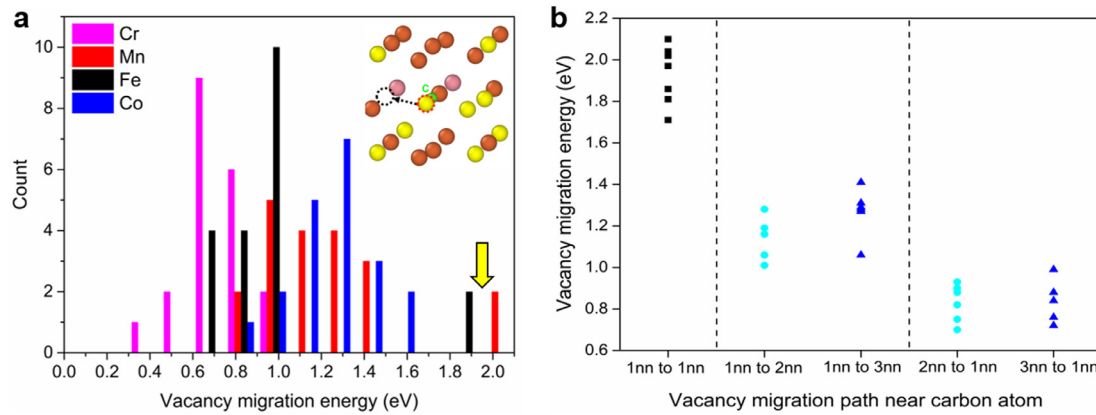


Fig. 14. (a) Vacancy migration energy for Fe_{49.5}Mn₃₀Co₁₀Cr₁₀C_{0.5} from first-principles calculations. The two large vacancy migration energies marked by the yellow arrow correspond to the vacancy jumps between the first nearest neighbors (1 nm) around the interstitial carbon atom. As illustrated in the inset image, the green atom corresponds to an interstitial carbon atom and the black arrow represents the vacancy migration between two 1 nm sites. (b) Variation in vacancy migration energy as a function of the migration direction of the vacancy site relative to the position of the interstitial carbon atom.

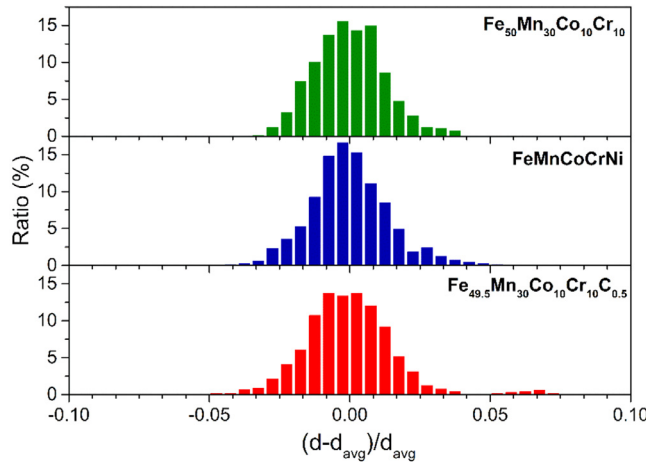


Fig. 15. The distribution of the nearest-neighbor distances for Fe₅₀Mn₃₀Co₁₀Cr₁₀, FeMnCoCrNi and Fe_{49.5}Mn₃₀Co₁₀Cr₁₀C_{0.5} obtained from first-principles calculations. The d_{avg} is the average nearest neighboring distances.

not only the density of dislocation loops, but also allows them to rapidly migrate to other dislocation loops to assist their growth, as shown in Fig. 9. Previous molecular dynamics studies also proved that increasing temperature or applying shear stress could facilitate the transformation of faulted loops into perfect loops [54].

As shown in Fig. 9d,e, FeMnCoCrNi has the highest density of dislocation loops and the largest fraction of faulted loops at all three temperatures. This is consistent with our previous finding that the incubation period for dislocation loop evolution is delayed with increasing chemical complexity [35]. The faulted loop contributes more to irradiation hardening than the perfect loop due to its sessile feature, as it has a Burgers vector of 1/3 <111> vertical to the slip planes. Thus, the high density of faulted loops will worsen irradiation hardening, which also means that extensive inhibition of dislocation loop growth is actually undesirable. For Fe_{49.5}Mn₃₀Co₁₀Cr₁₀C_{0.5}, when <112> Shockley partials slips on the <110> plane, the interstitial carbon atoms dissolved in the matrix readily meet and interact with them, resulting in most of them rapidly blocked and trapped, which decreases the mean free path of dislocations and therefore increases the stacking fault energy in the system [55,56]. In addition, unfaulting reaction of dislocation loops would prefer to occur if the following condition is satisfied

Table 2
Average vacancy migration energy from first-principles calculations.

Vacancy migration energy (eV)	Fe	Mn	Co	Cr	Ni
Fe _{49.5} Mn ₃₀ Co ₁₀ Cr ₁₀ C _{0.5}	1.19	0.99	1.31	0.70	
FeMnCoCrNi	0.79	0.69	1.20	0.96	1.21

[53,57]:

$$\gamma > \frac{Ga^2}{24\pi r} \cdot \frac{2-\nu}{1-\nu} \ln\left(\frac{2r}{r_c}\right), \quad (5)$$

where γ is the stacking fault energy, G is the shear modulus, a is the lattice constant, ν is the Poisson's ratio, r_c is the dislocation core radius, and r is the faulted loop radius. This means that higher stacking fault energy contributes to the higher probability of unfaulting reaction [36,58]. Thus, as shown in Fig. 9e, interstitial carbon atoms reduce the proportion of small faulted loops and promote the unfaulting reactions to form perfect loops, which could effectively reduce the ratio of faulted loops and mitigate irradiation hardening.

4.3. Suppressed radiation-induced segregation by interstitial carbon atoms

Radiation-induced segregation tends to form in the region of defect sinks, such as grain boundaries, cavities and dislocation loops. Diffusive fluxes of interstitial and vacancy to the defect sink often creates a concomitant preferential fluxes of atoms and lead to the redistribution of elements [59]. The RIS behavior in the vicinity of dislocation loops, one of the most typical two-dimensional radiation defects, is worth exploring due to the elemental complexity of high entropy alloys. The inverse Kirkendall mechanism, which governs the segregation behavior at sinks mainly due to the differences of vacancy-mediated diffusion, is usually responsible for RIS behavior in materials [59]. In this study, the vacancy migration energies in Fe_{49.5}Mn₃₀Co₁₀Cr₁₀C_{0.5} and FeMnCoCrNi [60] were obtained by first-principles calculations, as presented in Table 2. It is found that the vacancy migration energy in Fe_{49.5}Mn₃₀Co₁₀Cr₁₀C_{0.5} is ordered as Co>Fe>Mn>Cr. Therefore, in the vicinity of the dislocation loops in the irradiated region, the slower vacancy diffusion through Fe and Co results in their enrichment, while the faster vacancy diffusion of Mn and Cr results in their depletion. This is consistent with the RIS experimental results on dislocation loops, as presented in Fig. 10. Furthermore, the ordering of the elemental vacancy migration energies in FeMn-

CoCrNi and the RIS behavior are also consistent with prior research [10,61,62].

To be noted, the oscillating “W-shaped” pattern was observed in RIS profiles. The “W-shaped” profile with a width of approximately 1 nm emerges around the center of the dislocation loop, as seen in Fig. 11a–c. It resembles the RIS behavior at the grain boundaries with low-dose irradiation [63–66]. However, to our best knowledge, due to the sub-nanometer scale, the “W-shaped” profile at dislocation loops was reported for the first time in HEAs. According to previous studies, the “W-shaped” is a transient state involving RIS and pre-irradiation thermal non-equilibrium segregation (TNES) diffusion in grain boundaries [59,63]. It means that segregation already exists in the pre-irradiation materials. Unlike grain boundaries, dislocation loops are formed only after irradiation. Hence, this model fails to explain the current work, and the observed “W-shaped” is solely caused by the irradiation. RIS at the defect cluster is a complex multi-factor coupling process that is influenced by irradiation dose, irradiation temperature, etc. It should be emphasized that the “W-shaped” profile on grain boundaries was relatively more difficult to form under the condition of high-temperature or high-dose irradiation previously [35,62]. Thus, we believe that this metastable state phenomenon arises when the driving forces between radiation-induced defect gradient and chemical gradient reach equilibrium. In the early stages of irradiation, the individual elements are gradually forced toward or away from the bulk to the dislocation loop with driving forces generated by the irradiation. Then an elemental species concentration gradient is formed, which peaks near the dislocation loop (<1 nm). This cumulative concentration gradient will provide a chemical driving force from the dislocation loop outward to counterbalance the partial defect flux. Fe and Cr formed the “W-shaped” profile in the vicinity of the dislocation loop in $\text{Fe}_{49.5}\text{Mn}_{30}\text{Co}_{10}\text{Cr}_{10}\text{C}_{0.5}$ and $\text{Fe}_{50}\text{Mn}_{30}\text{Co}_{10}\text{Cr}_{10}$ alloys, whereas Ni and Cr showed this type of variation in FeMnCoCrNi . It indicates that the “W-shaped” elemental profile is also related to the alloy composition. A more systematic study needs to be carried out in association with molecular dynamics and rate theory [64,67], which is beyond the scope of our present study. The sub-nanometer “W-shaped” elemental distribution modifies the stacking fault energy around the dislocation loop by changing the local atomic configuration [68], thus affecting the evolutionary behavior of the dislocation loop. In addition, the scale of such localized elemental fluctuations is similar to the scale of concentration fluctuations in HEAs [69], and thus will inevitably modify the local lattice friction stress for dislocations and dislocation loops interactions during material deformation [70]. Therefore, we propose that the phenomenon of “W-shaped” around the dislocation loop has an impact on the mechanical behavior of the material in service. Furthermore, the unique segregation would also change the sink bias [71] to affect the local recombination of interstitial atoms and vacancies near dislocation loops. Thus, this sub-nanometer-scale elemental fluctuation around the dislocation loops provides new insight into the understanding of the long-term evolution of defects.

Lu et al. discovered that increasing number of elements in SP-CSA effectively suppresses RIS in the dislocation loop, which they ascribe to the slow atom transport originating from the higher number of principal elements [35]. In contrast, He et al. showed that the benefit for RIS suppression does not necessarily increase monotonically with the increase of the number of elements based on the observation that NiCoFeCr has a weaker RIS than FeMnCoCrNi at an irradiation temperature of 400 °C [10]. However, the impact of small interstitial atoms on RIS behavior in high-entropy alloys is still unknown. As can be seen in Fig. 14a, the vacancy migration energy of elements near the interstitial carbon atoms is significantly increased, which leads to a decrease in the vacancy diffusion rate and a reduction in the vacancy flux to the defect.

In addition, the local stress field induced by carbon interstitials can operate as defect recombination centers to reduce residual defect concentration [72], and disperse and annihilate the defect flux flowing to the dislocation loops. Thus, as shown in Fig. 11d, adding interstitial carbon atoms to HEA has a more pronounced suppression effect on the RIS behavior at dislocation loops.

Moreover, the RIS around the He bubbles was characterized on $\text{Fe}_{49.5}\text{Mn}_{30}\text{Co}_{10}\text{Cr}_{10}\text{C}_{0.5}$ in Fig. 12. At the surface of the He bubble, a ring-like segregation is formed. It might be attributed to the lowest configuration energy created by the redistribution of elements towards the He bubble, due to the difference in element size and affinity with He atoms [35]. It is also found that both He bubbles and dislocation loops exhibit similar RIS behavior, which could be explained by the dominance of the vacancy diffusion mechanism. Further atomic transport simulations calculations are needed to confirm this conjecture and clarify the difference in the segregation dynamics between He bubbles and dislocation loops.

4.4. Mitigated radiation-induced hardening effect by interstitial carbon atoms

Irradiation hardening is a useful tool to determine the mechanical behavior of materials with radiation-induced microstructures. The depth of the irradiated layer is only about 1200 nm, so the hardness after irradiation is revealed by a nanoindentation test. Moreover, the dispersed barrier-hardening (DBH) model can be used to characterize the incremental yield strength due to radiation-induced defects (dislocation loop, void, etc.), which is shown as follows [73]:

$$\Delta\sigma_y = \alpha M \mu b \sqrt{Nd}, \quad (6)$$

where $\Delta\sigma_y$ represents the increment of yield strength derived from the interaction of defect size d , number density N , strength α and Taylor factor M . The strength factor α depends on the types of defects [53], which could account for the minor increase in hardening as irradiation temperature increases for these three materials. In fact, the irradiated defects involve many black dots and vacancy-type stacking fault tetrahedra when the irradiation temperature is low (350 °C), as shown in Fig. S2, and their strength factors are smaller than those of dislocation loops and He bubbles. This may be the reason for the increase in hardening with irradiation temperature in the $\text{Fe}_{49.5}\text{Mn}_{30}\text{Co}_{10}\text{Cr}_{10}\text{C}_{0.5}$.

As seen in Fig. 13d, due to the higher chemical complexity, FeMnCoCrNi has the most pronounced hardening, which is consistent with prior studies [9]. On the contrary, the hardening of $\text{Fe}_{49.5}\text{Mn}_{30}\text{Co}_{10}\text{Cr}_{10}\text{C}_{0.5}$ is significantly mitigated by the addition of interstitial carbon atoms. This is attributed to a reduced overall hardening contribution from the effects of He bubbles and dislocation loops in $\text{Fe}_{49.5}\text{Mn}_{30}\text{Co}_{10}\text{Cr}_{10}\text{C}_{0.5}$. Thus, the interstitial carbon atoms promote the balanced evolution of various microstructures after irradiation. In summary, the interstitial carbon atoms alleviate both the hardening and volumetric swelling in the irradiated high-entropy alloy. $\text{Fe}_{49.5}\text{Mn}_{30}\text{Co}_{10}\text{Cr}_{10}\text{C}_{0.5}$ has both better tolerance to volumetric swelling and radiation-induced hardening than FeMnCoCrNi and $\text{Fe}_{50}\text{Mn}_{30}\text{Co}_{10}\text{Cr}_{10}$.

5. Conclusion

This work investigates the irradiation behavior of $\text{Fe}_{50}\text{Mn}_{30}\text{Co}_{10}\text{Cr}_{10}$, $\text{Fe}_{49.5}\text{Mn}_{30}\text{Co}_{10}\text{Cr}_{10}\text{C}_{0.5}$ and FeMnCoCrNi with increasing temperatures from 350 °C to 450 °C, focusing on the effect of radiation-induced defects evolution (He bubbles and dislocation loops) with particular regard to the role of interstitial carbon atoms.

- The variation of He bubble density and size distribution with temperature for the $\text{Fe}_{50}\text{Mn}_{30}\text{Co}_{10}\text{Cr}_{10}$, $\text{Fe}_{49.5}\text{Mn}_{30}\text{Co}_{10}\text{Cr}_{10}\text{C}_{0.5}$

and FeMnCoCrNi has been characterized by TEM. The interstitial atoms increase the local lattice distortion and restrain the vacancy diffusion, thus enhancing the recombination of radiation-induced point defects and inhibiting the formation of He bubbles, which results in the lowest volumetric swelling of $\text{Fe}_{49.5}\text{Mn}_{30}\text{Co}_{10}\text{Cr}_{10}\text{C}_{0.5}$ among the three studied HEAs.

- The interstitial carbon atoms act as sinks to disperse and annihilate partial defect flux, lessening the RIS at the dislocation loops in $\text{Fe}_{49.5}\text{Mn}_{30}\text{Co}_{10}\text{Cr}_{10}\text{C}_{0.5}$. Furthermore, it also increases the stacking fault energy, facilitating the transition from faulted loop to perfect loop.
- There is a “W-shaped” oscillatory pattern around the dislocation loop due to irradiation-induced segregation, thus providing new insight into the understanding the elemental redistribution around the dislocation loop and the interaction between defects during material deformation.
- The evolution of various defect microstructures is balanced by the interstitial carbon atoms. It reduces both radiation-induced hardening and volumetric swelling, paving the foundation for designing materials for nuclear applications.

Declaration of Competing Interest

The authors declare that they have no known competing financial interests or personal relationships that could have appeared to influence the work reported in this paper.

Acknowledgments

This work is supported by the National Key Research and the Development Program of China under Grant No. 2019YFA0209900; the National Natural Science Foundation of China under Grant Nos. 12075179 and 12105219; the China Postdoctoral Science Foundation under Grant No. 2021M702583; Guangdong Basic and Applied Basic Research Foundation under Grant No. 2020B1515120035. In addition, we thank Instrument Analysis Center of Xi'an Jiaotong University for TEM characterization.

Supplementary materials

Supplementary material associated with this article can be found, in the online version, at doi:10.1016/j.actamat.2022.117955.

References

- Z. Li, K.G. Pradeep, Y. Deng, D. Raabe, C.C. Tasan, Metastable high-entropy dual-phase alloys overcome the strength-ductility trade-off, *Nature* 534 (7606) (2016) 227–230.
- Z. Lei, X. Liu, Y. Wu, H. Wang, S. Jiang, S. Wang, X. Hui, Y. Wu, B. Gault, P. Konstis, D. Raabe, L. Gu, Q. Zhang, H. Chen, H. Wang, J. Liu, K. An, Q. Zeng, T.G. Nieh, Z. Lu, Enhanced strength and ductility in a high-entropy alloy via ordered oxygen complexes, *Nature* 563 (7732) (2018) 546–550.
- T. Shi, P.H. Lei, X. Yan, J. Li, Y.D. Zhou, Y.P. Wang, Z.X. Su, Y.K. Dou, X.F. He, D. Yun, Current development of body-centered cubic high-entropy alloys for nuclear applications, *Tungsten* 3 (2) (2021) 197–217.
- P. Wu, K. Gan, D. Yan, Z. Fu, Z. Li, A non-equiautomic FeNiCoCr high-entropy alloy with excellent anti-corrosion performance and strength-ductility synergy, *Corros. Sci.* 183 (2021) 109341.
- H. Luo, S.S. Sohn, W. Lu, L. Li, X. Li, C.K. Soundararajan, W. Krieger, Z. Li, D. Raabe, A strong and ductile medium-entropy alloy resists hydrogen embrittlement and corrosion, *Nat. Commun.* 11 (1) (2020) 3081.
- E.P. George, D. Raabe, R.O. Ritchie, High-entropy alloys, *Nat. Rev. Mater.* 4 (8) (2019) 515–534.
- C. Lu, L. Niu, N. Chen, K. Jin, T. Yang, P. Xiu, Y. Zhang, F. Gao, H. Bei, S. Shi, Enhancing radiation tolerance by controlling defect mobility and migration pathways in multicomponent single-phase alloys, *Nat. Commun.* 7 (2016) 13564.
- Y. Zhang, G.M. Stocks, K. Jin, C. Lu, H. Bei, B.C. Sales, L. Wang, L.K. Béland, R.E. Stoller, G.D. Samolyuk, Influence of chemical disorder on energy dissipation and defect evolution in concentrated solid solution alloys, *Nat. Commun.* 6 (2015) 8736.
- K. Jin, C. Lu, L. Wang, J. Qu, W. Weber, Y. Zhang, H. Bei, Effects of compositional complexity on the ion-irradiation induced swelling and hardening in Ni-containing equiautomic alloys, *Scr. Mater.* 119 (2016) 65–70.
- M.R. He, S. Wang, S. Shi, K. Jin, H. Bei, K. Yasuda, S. Matsumura, K. Higashida, I.M. Robertson, Mechanisms of radiation-induced segregation in Cr-FeCoNi-based single-phase concentrated solid solution alloys, *Acta Mater.* 126 (2017) 182–193.
- N. Jia, Y. Li, H. Huang, S. Chen, D. Li, Y. Dou, X. He, W. Yang, Y. Xue, K. Jin, Helium bubble formation in refractory single-phase concentrated solid solution alloys under MeV He ion irradiation, *J. Nucl. Mater.* 550 (2021) 152937.
- T.X. Li, J.W. Miao, E.Y. Guo, H. Huang, J. Wang, Y.P. Lu, T.M. Wang, Z.Q. Cao, T.J. Li, Tungsten-containing high-entropy alloys: a focused review of manufacturing routes, phase selection, mechanical properties, and irradiation resistance properties, *Tungsten* 3 (2) (2021) 181–196.
- Z. Li, C.C. Tasan, H. Springer, B. Gault, D. Raabe, Interstitial atoms enable joint twinning and transformation induced plasticity in strong and ductile high-entropy alloys, *Sci. Rep.* 7 (2017) 40704.
- Z. Li, Interstitial equiautomic CoCrFeMnNi high-entropy alloys: carbon content, microstructure, and compositional homogeneity effects on deformation behavior, *Acta Mater.* 164 (2019) 400–412.
- W. Lu, C.H. Liebscher, F. Yan, X. Fang, L. Li, J. Li, W. Guo, G. Dehm, D. Raabe, Z. Li, Interfacial nanophases stabilize nanotwins in high-entropy alloys, *Acta Mater.* 185 (2020) 218–232.
- X. Wang, Q. Yan, G.S. Was, L. Wang, Void swelling in ferritic-martensitic steels under high dose ion irradiation: exploring possible contributions to swelling resistance, *Scr. Mater.* 112 (2016) 9–14.
- Y. Satoh, H. Matsui, T. Hamaoka, Effects of impurities on one-dimensional migration of interstitial clusters in iron under electron irradiation, *Phys. Rev. B* 77 (9) (2008) 094135.
- S. Shen, F. Chen, X. Tang, J. Lin, G. Ge, J. Liu, Effects of carbon doping on irradiation resistance of $\text{Fe}_{38}\text{Mn}_{40}\text{Ni}_{11}\text{Al}_4\text{Cr}_7$ high entropy alloys, *J. Nucl. Mater.* 540 (2020) 152380.
- E. Lu, I. Makkonen, K. Mizohata, Z. Li, J. Räisänen, F. Tuomisto, Effect of interstitial carbon on the evolution of early-stage irradiation damage in equi-atomic FeMnNiCoCr high-entropy alloys, *J. Appl. Phys.* 127 (2) (2020) 025103.
- E. Lu, J. Zhao, I. Makkonen, K. Mizohata, Z. Li, M. Hua, F. Djurabekova, F. Tuomisto, Enhancement of vacancy diffusion by C and N interstitials in the equiautomic FeMnNiCoCr high entropy alloy, *Acta Mater.* 215 (2021) 117093.
- D.J.M. King, S.T.Y. Cheung, S.A. Humphry-Baker, C. Parkin, A. Couet, M.B. Cortie, G.R. Lumpkin, S.C. Middleburgh, A.J. Knowles, High temperature, low neutron cross-section high-entropy alloys in the Nb-Ti-V-Zr system, *Acta Mater.* 166 (2019) 435–446.
- T. Shi, Z. Su, J. Li, C. Liu, J. Yang, X. He, D. Yun, Q. Peng, C. Lu, Distinct point defect behaviours in body-centered cubic medium-entropy alloy NbZrTi induced by severe lattice distortion, *Acta Mater.* 229 (2022) 117806.
- C. Liu, W. Lu, W. Xia, C. Du, Z. Rao, J.P. Best, S. Brinckmann, J. Lu, B. Gault, G. Dehm, G. Wu, Z. Li, D. Raabe, Massive interstitial solid solution alloys achieve near-theoretical strength, *Nat. Commun.* 13 (1) (2022) 1102.
- J. Su, D. Raabe, Z. Li, Hierarchical microstructure design to tune the mechanical behavior of an interstitial TRIP-TWIP high-entropy alloy, *Acta Mater.* 163 (2019) 40–54.
- S. Yang, Y. Yang, Thermodynamics-kinetics of twinning/martensitic transformation in $\text{Fe}_{50}\text{Mn}_{30}\text{Co}_{10}\text{Cr}_{10}$ high-entropy alloy during adiabatic shearing, *Scr. Mater.* 181 (2020) 115–120.
- T.N. Yang, C. Lu, G. Velisa, K. Jin, P. Xiu, Y. Zhang, H. Bei, L. Wang, Influence of irradiation temperature on void swelling in NiCoFeCrMn and NiCoFeCrPd, *Scr. Mater.* 158 (2019) 57–61.
- W.J. Weber, Y. Zhang, Predicting damage production in monoatomic and multi-elemental targets using stopping and range of ions in matter code: challenges and recommendations, *Curr. Opin. Solid State Mater. Sci.* 23 (4) (2019) 100757.
- M. Norgett, M. Robinson, I. Torrens, Standard practice for neutron radiation damage simulation by charged-particle irradiation, *Annual Book of ASTM Standards* 12.02 (2016).
- P. Xiu, H. Bei, Y. Zhang, L. Wang, K.G. Field, STEM characterization of dislocation loops in irradiated FCC alloys, *J. Nucl. Mater.* 544 (2021) 152658.
- J. Hafner, Ab-initio simulations of materials using VASP: density-functional theory and beyond, *J. Comput. Chem.* 29 (13) (2008) 2044–2078.
- M. Ernzerhof, G.E. Scuseria, Assessment of the Perdew-Burke-Ernzerhof exchange-correlation functional, *J. Chem. Phys.* 110 (11) (1999) 5029–5036.
- A. Zunger, S.H. Wei, L. Ferreira, J.E. Bernard, Special quasirandom structures, *Phys. Rev. Lett.* 65 (3) (1990) 353.
- G. Henkelman, B.P. Uberuaga, H. Jónsson, A climbing image nudged elastic band method for finding saddle points and minimum energy paths, *J. Chem. Phys.* 113 (22) (2000) 9901–9904.
- W. Tang, E. Sanville, G. Henkelman, A grid-based Bader analysis algorithm without lattice bias, *J. Phys. Condens. Matter* 21 (8) (2009) 084204.
- C. Lu, T. Yang, K. Jin, N. Gao, P. Xiu, Y. Zhang, F. Gao, H. Bei, W.J. Weber, K. Sun, Y. Dong, L. Wang, Radiation-induced segregation on defect clusters in single-phase concentrated solid-solution alloys, *Acta Mater.* 127 (2017) 98–107.
- T. Yang, W. Guo, J.D. Poplawsky, D. Li, L. Wang, Y. Li, W. Hu, M.L. Crespiello, Z. Yan, Y. Zhang, Y. Wang, S.J. Zinkle, Structural damage and phase stability of $\text{Al}_{0.3}\text{CoCrFeNi}$ high entropy alloy under high temperature ion irradiation, *Acta Mater.* 188 (2020) 1–15.
- W.D. Nix, H. Gao, Indentation size effects in crystalline materials: a law for strain gradient plasticity, *J. Mech. Phys. Solids* 46 (3) (1998) 411–425.
- X. Zhang, K. Hattar, Y. Chen, L. Shao, J. Li, C. Sun, K. Yu, N. Li, M.L. Taheri, H. Wang, J. Wang, M. Nastasi, Radiation damage in nanostructured materials, *Prog. Mater. Sci.* 96 (2018) 217–321.

- [39] G.R. Odette, M.J. Alinger, B.D. Wirth, Recent developments in irradiation-resistant steels, *Annu. Rev. Mater. Res.* 38 (1) (2008) 471–503.
- [40] D. Chen, Y. Tong, H. Li, J. Wang, Y.L. Zhao, A. Hu, J.J. Kai, Helium accumulation and bubble formation in FeCoNiCr alloy under high fluence He⁺ implantation, *J. Nucl. Mater.* 501 (2018) 208–216.
- [41] D. Chen, S. Zhao, J. Sun, P. Tai, Y. Sheng, G. Yeli, Y. Zhao, S. Liu, W. Lin, W. Kai, Effects of minor alloying addition on He bubble formation in the irradiated FeCoNiCr-based high-entropy alloys, *J. Nucl. Mater.* 542 (2020) 152458.
- [42] X. Wang, C. Hatzoglou, B. Snead, Z. Fan, W. Guo, K. Jin, D. Chen, H. Bei, Y. Wang, W.J. Weber, Interpreting nanovoids in atom probe tomography data for accurate local compositional measurements, *Nat. Commun.* 11 (1) (2020) 1–11.
- [43] F. Granberg, X. Wang, D. Chen, K. Jin, Y. Wang, H. Bei, W.J. Weber, Y. Zhang, K.L. More, K. Nordlund, F. Djurabekova, Origin of increased helium density inside bubbles in Ni_{1-x}Fe alloys, *Scr. Mater.* 191 (2021) 1–6.
- [44] X. Wang, K. Jin, D. Chen, H. Bei, Y. Wang, W.J. Weber, Y. Zhang, K.L. More, Effects of Fe concentration on helium bubble formation in NiFe_x single-phase concentrated solid solution alloys, *Materialia* 5 (2019) 100183.
- [45] C. Domain, C. Becquart, J. Foct, Ab initio study of foreign interstitial atom (C, N) interactions with intrinsic point defects in α -Fe, *Phys. Rev. B* 69 (14) (2004) 144112.
- [46] H. Trinkaus, B.N. Singh, Helium accumulation in metals during irradiation – where do we stand? *J. Nucl. Mater.* 323 (2–3) (2003) 229–242.
- [47] Y. Tong, S. Zhao, K. Jin, H. Bei, J.Y.P. Ko, Y. Zhang, F.X. Zhang, A comparison study of local lattice distortion in Ni₈₀Pd₂₀ binary alloy and FeCoNiCrPd high-entropy alloy, *Scr. Mater.* 156 (2018) 14–18.
- [48] Y. Tong, G. Velisa, S. Zhao, W. Guo, T. Yang, K. Jin, C. Lu, H. Bei, J. Ko, D. Pagan, Evolution of local lattice distortion under irradiation in medium-and high-entropy alloys, *Materialia* 2 (2018) 73–81.
- [49] H.S. Oh, K. Odbadrakh, Y. Ikeda, S. Mu, F. Körmann, C.J. Sun, H.S. Ahn, K.N. Yoon, D. Ma, C.C. Tasan, Element-resolved local lattice distortion in complex concentrated alloys: an observable signature of electronic effects, *Acta Mater.* 216 (2021) 117135.
- [50] H.S. Oh, S.J. Kim, K. Odbadrakh, W.H. Ryu, K.N. Yoon, S. Mu, F. Kormann, Y. Ikeda, C.C. Tasan, D. Raabe, T. Egami, E.S. Park, Engineering atomic-level complexity in high-entropy and complex concentrated alloys, *Nat. Commun.* 10 (1) (2019) 2090.
- [51] Y. Zhang, Y.N. Ossetsky, W.J. Weber, Tunable chemical disorder in concentrated alloys: defect physics and radiation performance, *Chem. Rev.* 122 (1) (2022) 789–829.
- [52] Z. Fan, S. Zhao, K. Jin, D. Chen, Y.N. Ossetsky, Y. Wang, H. Bei, K.L. More, Y. Zhang, Helium irradiated cavity formation and defect energetics in Ni-based binary single-phase concentrated solid solution alloys, *Acta Mater.* 164 (2019) 283–292.
- [53] G.S. Was, Fundamentals of Radiation Materials Science: Metals and Alloy, Fundamentals of Radiation Materials Science: Metals and Alloy, Springer, 2016.
- [54] T. Kadoyoshi, H. Kaburaki, F. Shimizu, H. Kimizuka, S. Jitsukawa, J. Li, Molecular dynamics study on the formation of stacking fault tetrahedra and unfaulting of Frank loops in FCC metals, *Acta Mater.* 55 (9) (2007) 3073–3080.
- [55] K. Gan, D. Yan, S. Zhu, Z. Li, Interstitial effects on the incipient plasticity and dislocation behavior of a metastable high-entropy alloy: nanoindentation experiments and statistical modeling, *Acta Mater.* 206 (2021) 116633.
- [56] Y. Ikeda, I. Tanaka, J. Neugebauer, F. Körmann, Impact of interstitial C on phase stability and stacking-fault energy of the CrMnFeCoNi high-entropy alloy, *Phys. Rev. Mater.* 3 (11) (2019) 113603.
- [57] D. Chen, Y. Tong, J. Wang, B. Han, Y.L. Zhao, F. He, J.J. Kai, Microstructural response of He⁺ irradiated FeCoNiCrTi_{0.2} high-entropy alloy, *J. Nucl. Mater.* 510 (2018) 187–192.
- [58] D. Hull, D.J. Bacon, *Introduction to Dislocations*, Elsevier, 2011.
- [59] A.J. Ardell, P. Bellon, Radiation-induced solute segregation in metallic alloys, *Curr. Opin. Solid State Mater. Sci.* 20 (3) (2016) 115–139.
- [60] W.M. Choi, Y.H. Jo, S.S. Sohn, S. Lee, B.J. Lee, Understanding the physical metallurgy of the CoCrFeMnNi high-entropy alloy: an atomistic simulation study, *NPJ Comput. Mater.* 4 (1) (2018) 1–9.
- [61] Z. Su, T. Shi, H. Shen, L. Jiang, L. Wu, M. Song, Z. Li, S. Wang, C. Lu, Radiation-assisted chemical short-range order formation in high-entropy alloys, *Scr. Mater.* 212 (2022) 114547.
- [62] W.Y. Chen, J.D. Poplawsky, Y. Chen, W. Guo, J.W. Yeh, Irradiation-induced segregation at dislocation loops in CoCrFeMnNi high entropy alloy, *Materialia* 14 (2020) 100951.
- [63] C.M. Barr, P.J. Felfer, J.I. Cole, M.L. Taheri, Observation of oscillatory radiation induced segregation profiles at grain boundaries in neutron irradiated 316 stainless steel using atom probe tomography, *J. Nucl. Mater.* 504 (2018) 181–190.
- [64] Y. Yang, K.G. Field, T.R. Allen, J.T. Busby, Roles of vacancy/interstitial diffusion and segregation in the microchemistry at grain boundaries of irradiated Fe–Cr–Ni alloys, *J. Nucl. Mater.* 473 (2016) 35–53.
- [65] E.A. Marquis, R. Hu, T. Rousseau, A systematic approach for the study of radiation-induced segregation/depletion at grain boundaries in steels, *J. Nucl. Mater.* 413 (1) (2011) 1–4.
- [66] T.G. Lach, M.J. Olszta, S.D. Taylor, K.H. Yano, D.J. Edwards, T.S. Byun, P.H. Chou, D.K. Schreiber, Correlative STEM-APT characterization of radiation-induced segregation and precipitation of in-service BWR 304 stainless steel, *J. Nucl. Mater.* 549 (2021) 152894.
- [67] X. Wang, H. Zhang, T. Baba, H. Jiang, C. Liu, Y. Guan, O. Elleuch, T. Kuech, D. Morgan, J.C. Idrobo, P.M. Voyles, I. Szlufarska, Radiation-induced segregation in a ceramic, *Nat. Mater.* 19 (9) (2020) 992–998.
- [68] S. Zhao, Y. Ossetsky, G.M. Stocks, Y. Zhang, Local-environment dependence of stacking fault energies in concentrated solid-solution alloys, *NPJ Comput. Mater.* 5 (1) (2019) 1–7.
- [69] Q. Ding, Y. Zhang, X. Chen, X. Fu, D. Chen, S. Chen, L. Gu, F. Wei, H. Bei, Y. Gao, M. Wen, J. Li, Z. Zhang, T. Zhu, R.O. Ritchie, Q. Yu, Tuning element distribution, structure and properties by composition in high-entropy alloys, *Nature* 574 (7777) (2019) 223–227.
- [70] J. Li, H. Chen, Q. Fang, C. Jiang, Y. Liu, P.K. Liaw, Unraveling the dislocation–precipitate interactions in high-entropy alloys, *Int. J. Plast.* 133 (2020) 102819.
- [71] M.A. Cusentino, M.A. Wood, R. Dingreville, Compositional and structural origins of radiation damage mitigation in high-entropy alloys, *J. Appl. Phys.* 128 (12) (2020) 125904.
- [72] Y. Zhang, Y.N. Ossetsky, W.J. Weber, Tunable chemical disorder in concentrated alloys: defect physics and radiation performance, *Chem. Rev.* 122 (1) (2021) 789–829.
- [73] B. Singh, A. Foreman, H. Trinkaus, Radiation hardening revisited: role of intra-cascade clustering, *J. Nucl. Mater.* 249 (2–3) (1997) 103–115.